RSC Advances

PAPER

View Article Online
View Journal | View Issue

Cite this: *RSC Adv.*, 2020, **10**, 28007

Structural, dielectric and impedance spectroscopy analysis of $Ba_5CaTi_{1.94}Zn_{0.06}Nb_8O_{30}$ ferroelectric ceramic

Amine Bendahhou, *[a] Karim Chourti,[a] Rachid El Bouayadi,[b] Soufian El Barkany[a] and Mohamed Abou-Salama [a]

In this work, Zn co-doped tungsten bronze having nominal formula $Ba_5CaTi_{1.94}Zn_{0.06}Nb_8O_{30}$ has been synthesized and systematically studied for structure, dielectric and electrical properties. The formation of the phase of tetragonal tungsten bronze with space group *P4bm* and the occurrence of oxygen vacancies were verified by the Rietveld refinement using X-ray diffraction data. Scanning electron microscopy (SEM) of $Ba_5CaTi_{1.94}Zn_{0.06}Nb_8O_{30}$ ceramic shows high densification, low porosity, and homogeneous distribution of grains of different sizes over the total surface. The sample shows a dielectric anomaly of ferroelectric paraelectric type at 262 °C, and has non-relaxor type of diffuse phase transition. The electrical property (complex impedance Z^*, complex permittivity ε^*, complex modulus M^*) of $Ba_5CaTi_{1.94}Zn_{0.06}Nb_8O_{30}$ ceramic has been investigated by non-destructive complex impedance spectroscopy (CIS) as a function of frequency at different temperatures. Grains and grain boundaries conduction is detected from a complex impedance spectrum by fitting the Nyquist plot with an appropriate electrical circuit. The Nyquist plot indicates the negative temperature coefficient of resistance (NTCR) character of $Ba_5CaTi_{1.94}Zn_{0.06}Nb_8O_{30}$ ceramic. The variation of AC conductivity as a function of frequency reveals that the compound has an Arrhenius-type behavior of electrical conductivity. The DC electrical conductivities of grains and grain boundaries have been studied. The presence of non-Debye relaxations was verified by a complex modulus analysis.

Received 12th June 2020
Accepted 17th July 2020

DOI: 10.1039/d0ra05163b

rsc.li/rsc-advances

1. Introduction

In recent years, tetragonal tungsten bronze (TTB) compounds have been extensively studied because they are part of an important family of dielectric materials, which exhibit interesting ferroelectric, pyroelectric and piezoelectric behaviors.[1–6] Tungsten–bronze compounds have been considered as candidates to replace lead-based compounds.[7,8] The (TTB) structure can be described as a complex chain of distorted BO_6 octahedra linked by their summits, leading to three different types of interstices (A1, A2 and C) with 12-, 15- and 9-fold coordination. Thus, their general formula is $[(A1)_2(A2)_4C_4][(B1)_2(B2)_8]O_{30}$. In the given formula, the A1 and A2 sites are mostly occupied by divalent or trivalent cations,[9,10] the B1 and B2 sites by tetravalent or pentavalent cations,[11,12] and the C site receive small cations such as Li^+,[13] (see the insets of Fig. 1). In our research, the site (C) is small and often remains empty, the general formula becomes $[(A1)_2(A2)_4][(B1)_2(B2)_8]O_{30}$. The wide variety of cationic sites (A1, A2, C, B1 and B2) leads to a great variety of structures, permitting the modification of the characteristics of the (TTB), by substitutions in the A1 and A2 sites or in the B1 and B2 octahedra. For example, the $M_{6-p}R_pTi_{2+p}Nb_{8-p}O_{30}$ ($p = 1.2$; M = Ba or Sr; R = rare earth) tetragonal tungsten bronze system, the difference in ion size between the A1 and A2 sites is an important factor in the transition from relaxant to normal ferroelectric.[4,14–16] $Ba_4R_2Ti_4Nb_6O_{30}$ (R = Bi, La) with a smaller ionic size difference exhibits relaxation behavior, whereas $Ba_4R_2Ti_4Nb_6O_{30}$ (R = Nd, Sm) with a larger size difference exhibits normal ferroelectric behavior. In addition, the creation of oxygen vacancy is also an effective method to improve the properties of the oxides, and it has attracted considerable attention to many oxides because of its close relationship to material properties.[17–19] Oxygen vacancy is one of the most important modifying factors that cannot be ignored for all oxide materials, they can be created by doping or atmospheric reduction.[20–22] However, there are few published studies on the effect of oxygen vacancies on the structure, dielectric, and electrical properties of (TTB) ceramics.[23–25] In our case, the Ti^{4+} ion, which is tetravalent, is substituted by Zn^{2+} which is bivalent. Thus, this heterogeneous substitution leads to a change in the charge of the "B1, and B2" sites, compensated by the creation of oxygen vacancies (OVs).

[a]*Department of Chemistry, Laboratory of Molecular Chemistry, Materials and Environment, Faculty Multidisciplinary Nador, University Mohamed Premier, B.P. 300, Selouane, Nador 62700, Morocco. E-mail: bendahhou_amine1718@ump.ac.ma*
[b]*ISET, ENSA, Ibn Tofayl University of Kénitra, 14000 Kénitra, Morocco*

Shilpi Jindal *et al.*,[26] studied structural and dielectrical properties of lead-free polycrystalline electro ceramics $Ba_5CaTi_2Nb_8O_{30}$ (BCTN) for microwave tunable device applications. They found that the ceramic $Ba_5CaTi_2Nb_8O_{30}$ (BCTN) was single-phase with a tungsten–bronze structure in space group *P4bm*. The lattice parameters of $Ba_5CaTi_2Nb_8O_{30}$ are calculated as: $a = 8.3311$ Å, $c = 12.1289$ Å, $V = 841.8334$ Å^3, the grain size of the BCTN ceramic was 6 μm and this compound has a dielectric anomaly at 316 °C which corresponds to the Curie temperature T_c.

The complex impedance spectroscopy (CIS) technique has been extensively used to study the physical processes determining the electrical and dielectric properties of materials. It is used to separate the contributions of grains and grain boundaries to the transport properties of materials.[27] CIS allows the evaluation of the relaxation frequency/relaxation time of charge carriers in the material, which is a characteristic property of the samples. CIS also allows the study of conductivity as a function of frequency, modulus spectra, relative permittivity and dielectric losses. The variation of impedance parameters as a function of frequency and temperature can be appropriately modelled with equivalent circuits, which will assist the researcher in determining the responsible physical processes.[28–33]

The present work is focused on the titanium–zinc substitution for compound of global composition $Ba_5CaTi_{1.94}Zn_{0.06}Nb_8O_{30}$ synthesized by standard solid-state reaction. The effect of the substitution of Ti by Zn on their structure, dielectric and electrical properties are studied in detail in this new tungsten bronze composition.

2. Materials and methods

$Ba_5CaTi_{1.94}Zn_{0.06}Nb_8O_{30}$ powder was synthesized by a classical solid-state route. The raw materials used are $BaCO_3$ (Sigma-Aldrich 99%), $CaCO_3$ (Aldrich 99.9%), Nb_2O_5 (Aldrich 99.9%), ZnO, (Himedia 99.9%) and TiO_2 (Sigma-Aldrich 99%). The raw powders were weighed in stoichiometric amounts and mixed in an agate mortar for 30 minutes. This powder was calcined in air at 1300 °C for 6 hours. The obtained powder was ground and mixed with polyvinyl alcohol (PVA) as a binder. Then, cylindrical pellet was obtained by pressing at 20 kN (12 mm diameter, 2 mm thickness). The green pellet was sintered at 1450 °C for 6 hours in air.

The identification of the crystalline structure of the $Ba_5CaTi_{1.94}Zn_{0.06}Nb_8O_{30}$ powder was performed by X-ray diffraction (XRD) using a $\theta/2\theta$ diffractometer fitted with a fast detector (Bruker D8, $CuK_{\alpha 1}$, Linkeye detector) at room temperature (293 K, 0.015° step, 10–120° 2θ range, scanning speed of 1° min^{-1}). The lattice parameters, atomic positions, occupation rate, and thermal agitation factor were refined by the Rietveld method using the Jana 2006 software.[34]

The sintered pellet was polished with a fine emery paper to make both surfaces flat and parallel and then annealed at 1300 °C for 30 min. The microstructure of $Ba_5CaTi_{1.94}Zn_{0.06}Nb_8O_{30}$ ceramic was checked by scanning electron microscopy (SEM) (TESCAN VEGA III LM), with an accelerating voltage of 10 kV. The average grain size of ceramic sample was estimated using Image J software. Before electrical measurements, the sintered ceramic was painted with silver paste and annealed for 30 minutes at 300 °C to adhere to the silver on the sample and then cooled to room temperature before taking any measurement. The disc shaped silver coated pellet behaves like a parallel plate capacitor which is used for various dielectric and electrical measurements. The relative permittivity, dielectric losses (tan δ), the real and imaginary part of impedance and phase angle were determined using a BioLogic impedance analyzer (MTZ-35) over the frequency range of 10 Hz to 1 MHz with an AC voltage amplitude of 1 V, the furnace and the sample

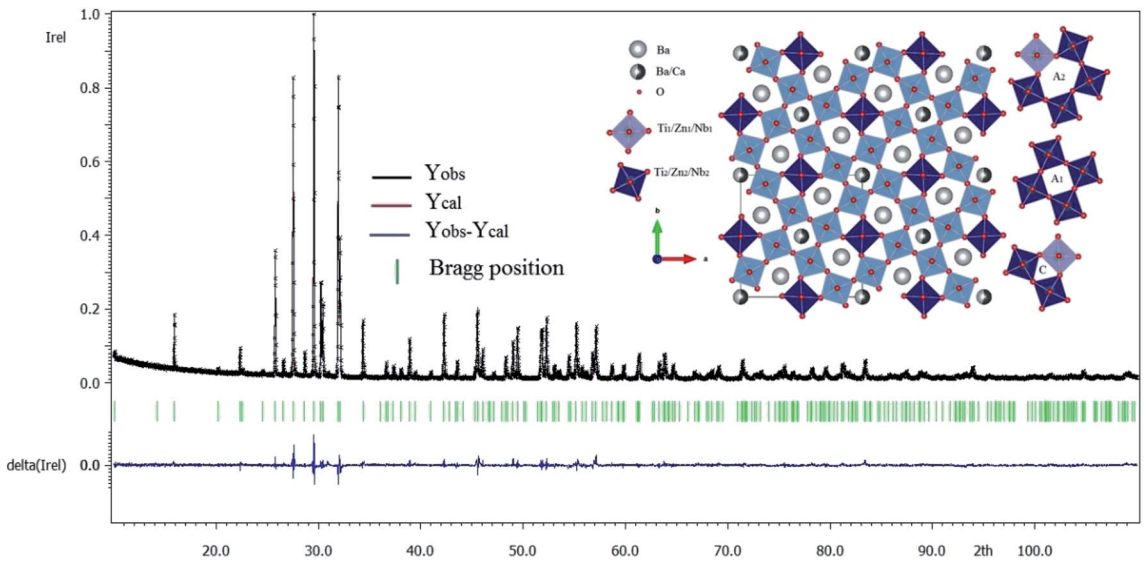

Fig. 1 X-ray diffraction refinement for $Ba_5CaTi_{1.94}Zn_{0.06}Nb_8O_{30}$ powder, and representation of the TTB structure of $Ba_5CaTi_{1.94}Zn_{0.06}Nb_8O_{30}$ along the "*c*" axis.

Table 1 Structural data for $Ba_5CaTi_{1.94}Zn_{0.06}Nb_8O_{30}$ powder and the experimental conditions

Crystallographic data	
Formula	$Ba_5CaTi_{1.94}Zn_{0.06}Nb_8O_{30}$
Crystal system	Tetragonal
Space group	*P4bm*
a (Å)	12.4631(6)
c (Å)	3.9812(2)
V (Å^3)	618.40(5)
Z	1
Density (g cm^{-3})	5.2681
Data collection	
Temperature (°C)	25
Wavelength [CuKα] (Å)	1.5406
Measuring range (°)	$10 \leq 2\theta \leq 120$
Step (2θ)	0.015
Rietveld data	
Program	Jana 2006
Profile function	Pseudo Voigt
Number of refined parameters	48
Caglioti parameters	$U = 0.113$; $V = 0.409$; $W = 0.015$
R_p (%)	6.52
R_{wp} (%)	8.67
R_{exp} (%)	4.99
GOF	1.74

temperatures were controlled by MT-lab software using a heat-up rate of 5 °C min^{-1}.

3. Results and discussion

3.1. Structural study

Fig. 1 gives the result of the Rietveld refinement of the XRD data for $Ba_5CaTi_{1.94}Zn_{0.06}Nb_8O_{30}$ powder. Refinement results indicate that the $Ba_5CaTi_{1.94}Zn_{0.06}Nb_8O_{30}$ ceramic was single-phase with a tungsten–bronze structure in space group *P4bm*.

The Fig. 1 shows a comparison of the observed data (black line) and calculated data (red line) from the X-ray patterns and the smallest difference between them (solid blue line) for $Ba_5CaTi_{1.94}Zn_{0.06}Nb_8O_{30}$. This difference between the calculated and measured data is the best method to confirm the quality and success of the refinement. According to the literature, the quality and validity of the various data from structural refinement have generally been verified by the reliability index parameters (R-values), *i.e.* R_p (R-profile), R_{wp} (R-weighted profile), R_{exp} (expected residual factor), and GOF (goodness of fit). The selected R-values are described as follows equations,

$$R_p = \frac{\sum_i |I_{obs} - I_{cal}|}{\sum_i I_{obs}} \quad (1)$$

$$R_{wp} = \left[\frac{\left(\sum_i w_i (I_{obs} - I_{cal})^2 \right)}{\left(\sum_i w_i {I_{obs}}^2 \right)} \right]^{\frac{1}{2}} \quad (2)$$

$$R_{exp} = \left[\frac{(N - P)}{\left(\sum_i w_i {I_{obs}}^2 \right)} \right]^{\frac{1}{2}} \quad (3)$$

$$GOF = \frac{R_{wp}}{R_{exp}} \quad (4)$$

where, I_{obs} and I_{cal} represents the experimental and calculated intensities of the reflections at angle $2\theta i$ and w_i is weight. N is the number of measuring points, P is the number of refined parameters. From the above equations, it is evident that the quality of fit (GOF) depends on R_{wp} and R_{exp}, and for the best fit of the Rietveld analysis, GOF the value should be less than 2.[35,36]

Good agreement between the calculated and observed model was obtained with $R_p = 6.52\%$, $R_{wp} = 8.67\%$, and GOF = 1.74. Table 1 gives the structural data for $Ba_5CaTi_{1.94}Zn_{0.06}Nb_8O_{30}$ powder, and experimental conditions. The refined structural parameters (atomic positions, occupation rate, and thermal agitation factor) are shown in Table 2. The selected bond distances and angles are summarized in Table 3. The insets of Fig. 1 represent the crystallographic structure along the c-axis for the composition $Ba_5CaTi_{1.94}Zn_{0.06}Nb_8O_{30}$. Ti^{4+}, Zn^{2+}, and Nb^{5+} occupy the B1 and B2 sites in a ratio of 1.94 : 0.06 : 8. Ba^{2+} sit in the A2 site (the pentagonal site), the residue of the Ba^{2+} with the Ca^{2+} occupy the A1 site (the square site) simultaneously with a ratio of 1 : 1.

The final chemical formula after the structural refinement step was $Ba_{4.745}Ca_{1.129}Ti_{2.953}Zn_{0.06}Nb_{6.987}O_{29.409}$ evidencing

Table 2 Refined structural parameters for $Ba_5CaTi_{1.94}Zn_{0.06}Nb_8O_{30}$ powder from X-ray diffraction data

Atom	Wyckoff position	x	y	z	B_{iso} (Å^2)	Occupies
Ca1/Ba1	2a	0	0	0	1.74(12)	0.56(4)/0.44(4)
Ba2	4c	0.17114(9)	0.67114(9)	0	2.78(8)	0.97(4)
Ti1/Zn1/Nb1	2b	0	0.50	0.501(3)	1.56(15)	0.37(6)/0.006/0.62(6)
Ti2/Zn2/Nb2	8d	0.07393(12)	0.21358(11)	0.495(3)	1.50(9)	0.28(7)/0.006/0.72(7)
O1	2b	0	0.50	0.048(13)	2.50(31)	0.9768
O2	4c	0.2856(6)	0.7856(6)	0.551(8)	2.50(31)	1.05(4)
O3	8d	0.0746(7)	0.2066(6)	0.024(10)	2.50(31)	0.94(3)
O4	8d	0.3443(8)	0.0061(6)	0.549(5)	2.50(31)	1.02(4)
O5	8d	0.1387(7)	0.0701(7)	0.564(5)	2.50(31)	0.95(3)

Table 3 Selected bond distances (Å) and angles (°) for $Ba_5CaTi_{1.94}Zn_{0.06}Nb_8O_{30}$

Bond distances (Å)		Bond angles (°)	
Ca(1)/Ba(1)–O(3)	2.740(8) × 4	O(1)–Ti(1)/Zn(1)/Nb(1)–O(1)	180.0(5)
Ca(1)/Ba(1)–O(5)	2.600(16) × 4	O(1)–Ti(1)/Zn(1)/Nb(1)–O(4)	84.3(7) × 4
	2.966(17) × 4		95.7(7) × 4
Ba(2)–O(2)	2.69(2) × 1	O(4)–Ti(1)/Zn(1)/Nb(1)–O(4)	85.0(3) × 2
	2.98(2) × 1		93.9(3) × 2
Ba(2)–O(4)	2.737(15) × 2		168.6(11) × 2
	3.007(16) × 2	O(2)–Ti(2)/Zn(2)/Nb(2)–O(3)	84.4(10)
			97.5(10)
Ti(1)/Zn(1)/Nb(1)–O(1)	1.80(5) × 1	O(2)–Ti(2)/Zn(2)/Nb(2)–O(4)	93.6(4)
	2.18(5) × 1	O(2)–Ti(2)/Zn(2)/Nb(2)–O(5)	91.9(4)
Ti(1)/Zn(1)/Nb(1)–O(4)	1.952(11) × 4		165.7(12)
		O(3)–Ti(2)/Zn(2)/Nb(2)–O(3)	175.0(3)
Ti(2)/Zn(2)/Nb(2)–O(2)	1.980(9) × 1	O(3)–Ti(2)/Zn(2)/Nb(2)–O(4)	85.7(7)
Ti(2)/Zn(2)/Nb(2)–O(3)	1.88(4) × 1		98.8(8)
	2.11(4) × 1	O(3)–Ti(2)/Zn(2)/Nb(2)–O(5)	79.8(7)
	1.922(10) × 1		81.4(7)
Ti(2)/Zn(2)/Nb(2)–O(4)	1.982(10) × 1		95.5(7)
Ti(2)/Zn(2)/Nb(2)–O(5)	2.041(10) × 1		96.8(7)
		O(4)–Ti(2)/Zn(2)/Nb(2)–O(5)	85.2(4)
			163.9(10)
		O(5)–Ti(2)/Zn(2)/Nb(2)–O(5)	85.8(4)

oxygen vacancies, this is attributed to the increase in the number of positive charges lost during the substitution of titanium by zinc and due to high sintering temperature (1450 °C).

The cations Ti, Zn, and Nb show clearly off-centre displacements along the *c*-axis in both $Ti/Zn/Nb(1)O_6$ and $Ti/Zn/Nb(2)O_6$ octahedra (Fig. 2(b)). The $Ti/Zn/Nb(1)O_6$ octahedra have four equal Ti/Zn/Nb(1)–O(4) bond length (see Table 3). In addition, the unequal Ti/Zn/Nb(2)–O bonds length of $Ti/Zn/Nb(2)O_6$ indicates the displacement of the cations Ti/Zn/Nb(2) in the *ab* plane, and no displacement of the cations Ti/Zn/Nb(1) occurs in the *ab* plane indicating more distortion in $Ti/Zn/Nb(2)O_6$ than in $Ti/Zn/Nb(1)O_6$ the octahedron. The arrows in Fig. 2(a) indicate the tilting direction for $Ti/Zn/Nb(2)O_6$ octahedron.

3.2. Microstructure of ceramic samples

Fig. 3(a) shows the SEM picture of the surface of $Ba_5CaTi_{1.94}Zn_{0.06}Nb_8O_{30}$ pellet sintered at 1450 °C for 6 hours, from which we can deduce that the compound has a dense microstructure and that the unequal grain sizes are homogeneously distributed over the entire surface of the sample. The relative density is 96% of the theoretical density. The histogram of Fig. 3(b) show that the average grain size for $Ba_5CaTi_{1.94}Zn_{0.06}Nb_8O_{30}$ceramic is 1.39 μm.

3.3. Study of dielectric properties

Complex impedance spectroscopy is a non-destructive technique allowing the determination of the relationships between dielectric properties, structure and microstructure. In this technique, during the measurement, four variables were stored as a function of frequencies which is the real and imaginary part of the impedance, the phase angle, and the dielectric loss.

The complex permittivity ε^* can be expressed in terms of real value (ε') and imaginary part (ε'').

$$\varepsilon^* = \varepsilon' - j\varepsilon''; \quad |\varepsilon^*| = \sqrt{(\varepsilon')^2 + (\varepsilon'')^2} \tag{5}$$

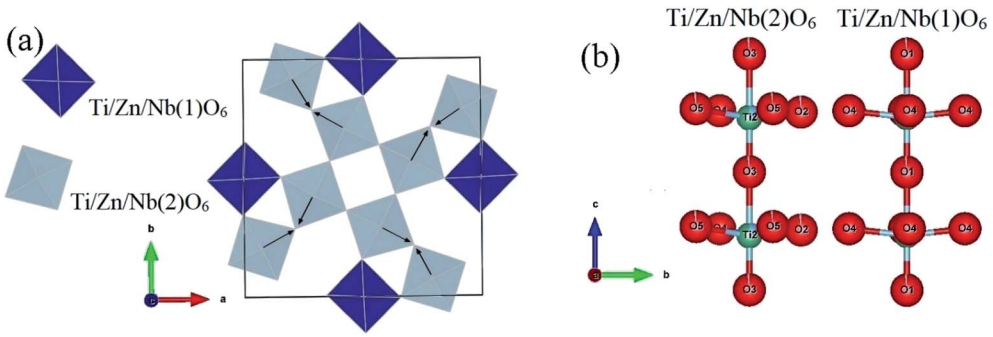

Fig. 2 (a) Polyhedral representation of $Ba_5CaTi_{1.94}Zn_{0.06}Nb_8O_{30}$ ceramic along the "*c*" axis. (b) Representation describing the distortions of the two kinds of octahedra in $Ba_5CaTi_{1.94}Zn_{0.06}Nb_8O_{30}$ ceramic along the "*a*" axis.

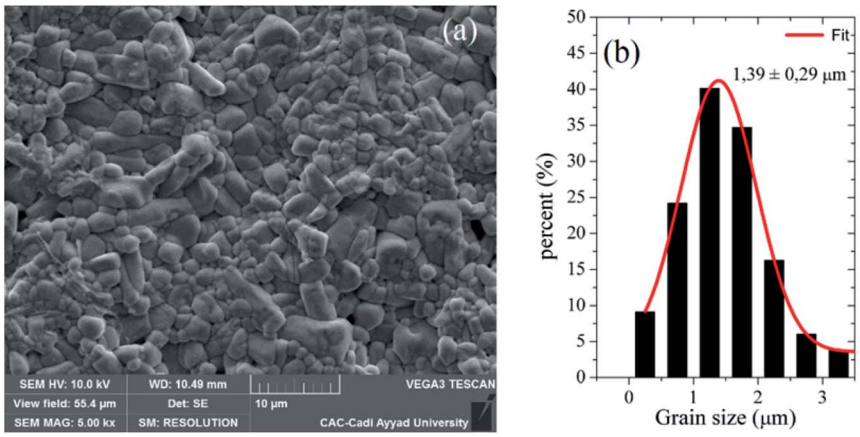

Fig. 3 (a) SEM picture of the surface of $Ba_5CaTi_{1.94}Zn_{0.06}Nb_8O_{30}$ ceramic, and (b) associated grain size distributions.

The relative permittivity (dielectric constant ε_r) and the dielectric losses (tan δ) were determined from complex impedance Z^* ($Z^* = Z' + jZ''$) data using the following expressions[37]

$$\varepsilon' = \frac{t}{\omega A \varepsilon_0} \times \frac{-Z''}{(Z')^2 + (Z'')^2}; \quad \varepsilon'' = \frac{t}{\omega A \varepsilon_0} \times \frac{Z'}{(Z')^2 + (Z'')^2}; \quad \tan\delta = \frac{\varepsilon''}{\varepsilon'} \tag{6}$$

where, $\omega = 2\pi f$ with f = frequency (Hz), A = pellet area (m^2), t = pellet thickness (m), ε_0 vacuum permittivity ($\varepsilon_0 = 8.85418782 \times 10^{-12}$ F m^{-1}), Z' = real part of the impedance and Z'' = imaginary part of the impedance.

Fig. 4(a) exhibits the variation of the dielectric constant (ε_r) of $Ba_5CaTi_{1.94}Zn_{0.06}Nb_8O_{30}$ ceramic measured at 10 Hz to 1 MHz. It can be seen that the dielectric constant decreases gradually as the frequency increases from 10 Hz to 100 Hz and it is almost constant at frequencies higher than 100 Hz. Everyone knows that as the frequency increases, the dielectric constant steadily decreases, which is a common characteristic of dielectric materials. The high permittivity in the low-frequency region is due to the different types of polarization present in these materials, such as dipole, atomic, ionic, electronic, *etc.*[9,38,39] For

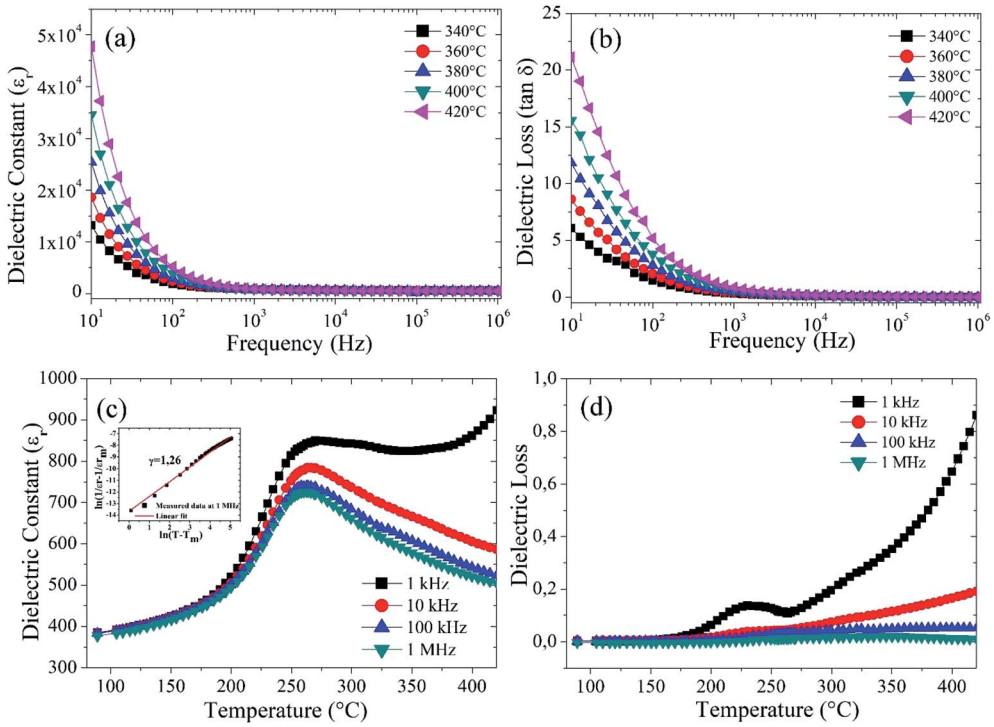

Fig. 4 (a) and (b) Frequency dependence of dielectric properties of $Ba_5CaTi_{1.94}Zn_{0.06}Nb_8O_{30}$ ceramic ranging from 10 Hz to 1 MHz. (c) and (d) Temperature dependence of the dielectric constant (ε_r) and dielectric loss (tan δ) for $Ba_5CaTi_{1.94}Zn_{0.06}Nb_8O_{30}$ ceramic respectively.

high frequencies, the relative permittivity decreases and reaches a plateau, this behavior indicates the occurrence of charged species (grain boundaries effect, oxygen vacancies…) which are incapable to follow the variation of the applied alternating electric field for high frequencies.

Fig. 4(b) shows the variation of the dielectric loss (tan δ) with frequency at different temperatures, it exhibits the same behavior as that of the dielectric constant (ε_r), *i.e.* decreasing with increasing frequency. This decline in dielectric losses (tan δ) with increasing frequency is attributed to the phenomenon of dipole relaxation.[40] The space charges are not capable to keep up with the high frequency of the applied electric field and go through relaxation. However, the origin of this behavior must be identified by complex impedance spectroscopy, in terms of analysis of the real and imaginary part of the complex impedance, analysis of the AC conductivity and study of the dielectric modulus.

From Fig. 4(c), It is found that the compound $Ba_5CaTi_{1.94}Zn_{0.06}Nb_8O_{30}$ has a dielectric anomaly at 262 °C (the Curie temperature T_c), suggesting the appearance of a ferroelectric to paraelectric phase transition. It is also observed that the compound has the same T_c for all frequencies (1 kHz to 1 MHz), indicating that $Ba_5CaTi_{1.94}Zn_{0.06}Nb_8O_{30}$ is a classical ferroelectric.[28] The dielectric peak is found to be broadened, indicating the existence of a diffuse phase transition.

The diffuse phase transition behavior of the dielectric constant can be evaluated using the modified Curie–Weiss equation[41,42]

$$\ln(1/\varepsilon_r - 1/\varepsilon_{rmax}) = \gamma \ln(T - T_{max}) + C_1 \quad (7)$$

where (ε_r) is the dielectric constant, (ε_{rmax}) is the peak value from ε_r to T_{max}, C_1 is the modified Weiss–Curie constant and (γ) is the diffusivity exponent. The value of γ calculated from the slope of the insets of Fig. 4(c) is found to be 1.26 at 1 MHz. The value (γ) is between 1 (normal ferroelectric and obeying Curie–Weiss law) and 2 (relaxing and completely disordered ferroelectric system), implying a diffuse ferroelectric nature of $Ba_5CaTi_{1.94}Zn_{0.06}Nb_8O_{30}$ ceramic. The defects such as oxygen vacancies give rise to disorders in the system,[43] which lead to a diffuse ferroelectric to paraelectric phase transition.

Fig. 4(d) shows the variation in dielectric loss (tan δ) for $Ba_5CaTi_{1.94}Zn_{0.06}Nb_8O_{30}$ ceramic at different frequencies. It shows a large peak in a temperature range from 190 °C to 280 °C. Such a wide maximum in (tan δ) results from the ferroelectric-to-paraelectric phase transition. The dielectric loss peak of $Ba_5CaTi_{1.94}Zn_{0.06}Nb_8O_{30}$ ceramic, which appears at a temperature below the dielectric constant, also exhibits a strong frequency dispersion.

3.4. Complex impedance analysis (CIA)

CIA using Nyquist plots allows the understanding of the effects of grains, grain boundaries and possible electrode effects on the capacitive, reactive, resistive and inductive properties of materials. Fig. 5(a) shows Nyquist plot for $Ba_5CaTi_{1.94}Zn_{0.06}Nb_8O_{30}$ ceramic at different temperatures, it shows that with increasing temperature, the Nyquist plot of $Ba_5CaTi_{1.94}Zn_{0.06}Nb_8O_{30}$ has a smaller semicircle, suggesting that the compound resistance

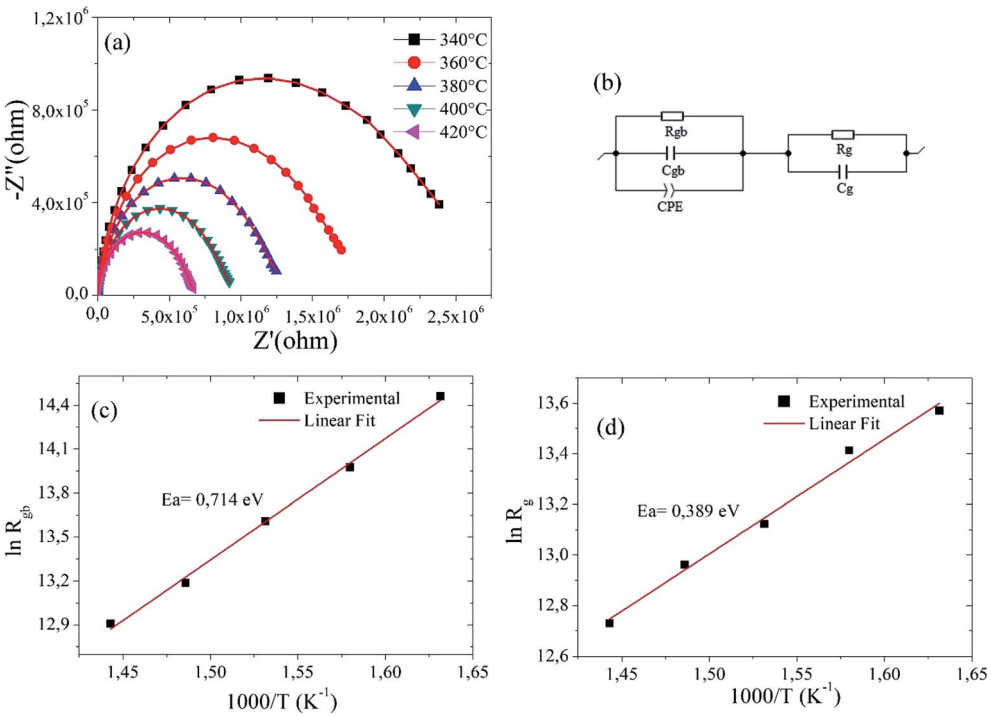

Fig. 5 (a) Nyquist plot fitted with an equivalent circuit for $Ba_5CaTi_{1.94}Zn_{0.06}Nb_8O_{30}$ ceramic at different temperatures. (b) Electrical equivalence circuit for the modeling of the impedance data. Arrhenius plot of the data obtained from the results of impedance circles; (c) for grain boundaries, and (d) for grains.

has progressively decreased. This resistance value has a strong effect on the amplitude of the real and imaginary part of the impedance.[44]

The equivalent circuit use to describe the electrical properties of the material is composed of two branches in series, which represent the electrical properties of the grains and the grain boundaries. In addition, the Z-View software can be utilized to adjust the parameters of each element in the equivalent circuit presenting in Fig. 5(b).

We used a series combination of two parallel circuits to characterize respectively the effect of grains and grain boundaries. In the first parallel circuit corresponding to the grain contribution, R_g and C_g correspond to the grain resistance and the grain capacitance. In the second parallel circuit, R_{gb}, C_{gb} and CPE were used as grain boundary resistance, grain boundary capacitance and constant phase element. A constant phase element CPE is introduced into the second circuit corresponding to the grain boundary properties due to the non-ideal capacitive behavior. This non-ideal grain boundary behavior can be due to the presence of more than one relaxation process.[45,46] The constant phase element (Q) is evaluated by the following relationship[20,47]

$$C = (R^{1-\alpha}Q)^{1/\alpha} \quad (8)$$

For an ideal resistor and an ideal capacitor, the value of (α) is zero and one, respectively.[48] A good agreement between the experimental data points and the theoretical line gives us confidence in the proposed equivalent circuit (see Fig. 5a). The various adjusted parameters are presented in Table 4.

The values of R_g and R_{gb} decrease with the increasing temperatures for $Ba_5CaTi_{1.94}Zn_{0.06}Nb_8O_{30}$ ceramic (see Table 4), showing the occurrence of a thermally activated conduction mechanisms in the grains and at the grain boundaries.

The relationship between resistance and temperature can be described by the Arrhenius equation

$$R = R_0 \exp(-E_a/K_BT) \quad (9)$$

where E_a is the activation energy for conduction, K_B is the Boltzmann's constant and R_0 is the pre-exponential factor and T the temperature (K). The E_g and E_{gb} values were calculated by linear fit presented in Fig. 5c and d, which were 0.389, and 0.714 eV, respectively. The higher activation energy values for the grain boundaries are probably related to the more disordered nature of the grain boundaries.

Table 4 Fitting parameters of the complex impedance plots at various temperatures for $Ba_5CaTi_{1.94}Zn_{0.06}Nb_8O_{30}$ ceramic

T (°C)	R_{gb} (MΩ)	C_{gb} (nF)	Q (nF $s^{\alpha-1}$)	α	R_g (Ω)	C_g (nF)
340	1.9086	0.4152	9.642	0.60959	782.87	0.9371
360	1.1724	0.4087	12.548	0.59569	669.05	0.8366
380	0.8127	0.3782	12.872	0.58587	500.41	0.8527
400	0.5329	0.3865	21.517	0.54298	425.69	0.7434
420	0.4061	0.4083	24.45	0.5238	335.37	0.6625

3.5. Electrical conductivity study

Conductivity values are calculated from the dielectric data using the relationship

$$\sigma_{AC} = \omega\varepsilon_0\varepsilon_r \tan\delta \quad (10)$$

where the symbols ε_0, ε_r, $\tan\delta$, ω, and σ_{AC} are respectively vacuum permittivity, relative permittivity, dielectric loss, angular frequency and AC conductivity.

In Fig. 6(a), the AC conductivity increases with increasing frequency for all temperatures. The AC conductivity at each measured temperature has two distinct regions. At low frequencies, a first region has been observed where the conductivity does not change with frequency. For the second region, the conductivity increases with increasing frequency. This type of AC conductivity can be explained by Jonscher's power law.[49]

$$\sigma_{AC} = \sigma_{DC} + A\omega^s \quad (11)$$

where the σ_{DC} indicates the DC conductivity and the second term is the frequency dependent AC conductivity, "A" is known as the polarizability force and "s" is the temperature dependent parameter. The variation of the "s" parameter with temperature is used to determine conduction mechanism. Funke has explained,[50] the physical importance of the numerical value of the "s". If $s \leq 1$, signifies that the hopping motion implies a translational motion with a sudden hopping, while $s > 1$, signifies that the motion implies a localized hopping without the species leaving the neighborhood. The insets of Fig. 6(a) showed the nonlinear curve fit to Jonscher's power law for $Ba_5CaTi_{1.94}Zn_{0.06}Nb_8O_{30}$ at 340 °C. The fitting parameters A, s, and σ_{DC} were calculated from the nonlinear fitting (Table 5).

From Table 5, it can be seen that with the rise in temperature, the strength of polarizability "A" increases, as confirmed by dielectric constant values of Fig. 4(a).

Fig. 6(b) gives the variation of the "s" parameter as a function of temperature (340–420 °C), demonstrating that "s" is varying inversely with temperature. This observation confirms that correlated barrier hopping (CBH) is the appropriate model to understand charge transport mechanism in this sample.[51] According to this model, AC conductivity in the sample $Ba_5CaTi_{1.94}Zn_{0.06}Nb_8O_{30}$ is due to the hopping of charge carriers between two sites over the potential barrier separating them, because of thermal activation.[52]

Fig. 6(c and d) shows the variation of $\ln(\sigma_{DC})$ with the inverse of the temperature ($10^3/T$), which gives the value of the activation energy for the electrical conduction of $Ba_5CaTi_{1.94}Zn_{0.06}Nb_8O_{30}$ ceramic at 1 kHz, which is calculated by Arrhenius law.

$$\sigma_{DC} = \sigma_0 \exp(-E_a/K_BT) \quad (12)$$

where k_B is the Boltzmann constant, σ_0 is the pre-exponential factor, T is the temperature (K) and E_a is the activation energy. The experimental data were fitted with the above equation (Fig. 6(c and d)). For the $Ba_5CaTi_{1.94}Zn_{0.06}Nb_8O_{30}$ ceramic, two activation energies were obtained at high

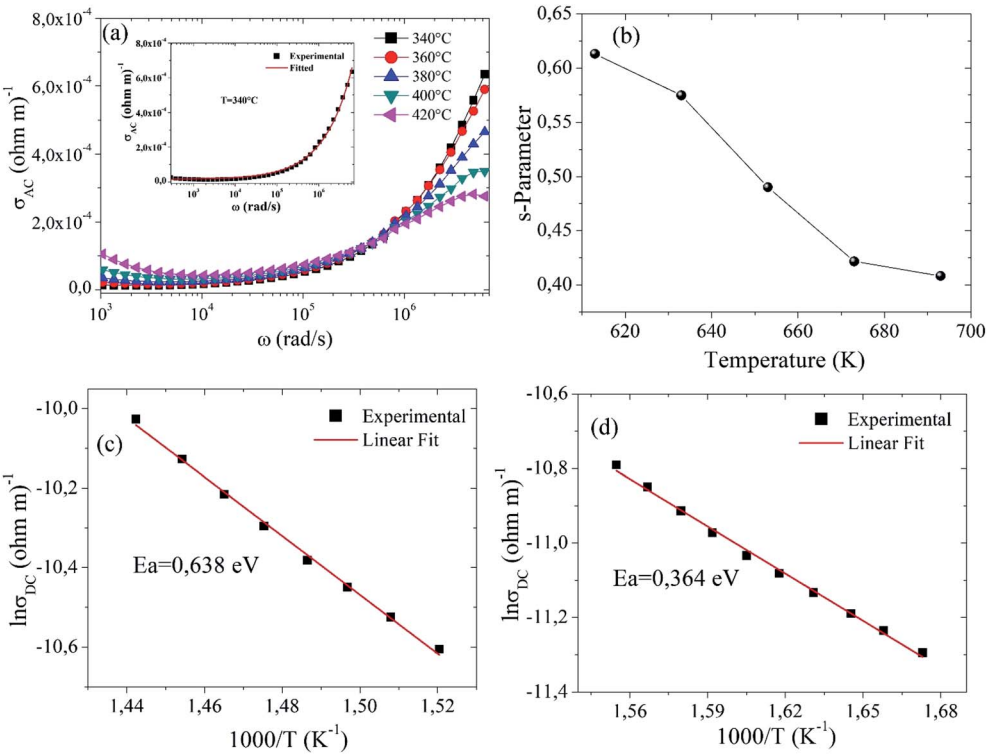

Fig. 6 (a) AC conductivity as a function of frequency. (b) Variation of *s*-parameter with temperature for $Ba_5CaTi_{1.94}Zn_{0.06}Nb_8O_{30}$ ceramic. (c), and (d) ln σ_{DC} as a function of $10^3/T$ for $Ba_5CaTi_{1.94}Zn_{0.06}Nb_8O_{30}$ ceramic for grain boundaries, and for grains at 1 kHz respectively.

temperature, which are the activation energies for grains and grain boundaries. It should be observed that the activation energy of the grain boundaries was higher than that of the grains. This means again that the grain boundaries have a higher resistance than the grains, as previously obtained from Nyquist plots (see Table 4).

In ferroelectric oxides, the thermal activation energy is strongly dependent on the concentration of oxygen vacancies (OVs).[10] A stoichiometric perovskite ABO_3 has an activation energy $E_a = 2$ eV, while the value of E_a is 1 eV for $ABO_{2.95}$ and 0.5 eV for $ABO_{2.90}$.[53,54]

The values of the activation energy E_a of the grain and the grain boundary are respectively 0.364 and 0.638 eV, suggesting that oxygen vacancies are responsible for the conduction mechanism in $Ba_5CaTi_{1.94}Zn_{0.06}Nb_8O_{30}$ ceramic. Furthermore, it is known that, the most mobile ionic species in ferroelectric oxides (perovskite, tungsten bronze lattice…) are the single and double ionized oxygen vacancies. It was often mentioned that the activation energy of single ionized OVs was about (0.3–0.5 eV) and about (0.6–1.2 eV) for double ionized OVs.[10]

Oxygen vacancies (OVs) can easily be formed in oxide materials by the loss of oxygen from the crystal lattice during heating at elevated temperatures (typically >1300 °C),[55] or in our case by the Ti^{4+}/Zn^{2+} substitution.

The oxygen vacancies creation can be explained by the Kröger–Vink defect equation

$$ZnO \xrightarrow{TiO_2} Zn_{Ti}^{//} + O_O^{\times} + V_O^{\cdot\cdot} \quad (13)$$

The single and double ionized oxygen vacancies will create the conducting electrons, written as

$$V_O \leftrightarrow V_O^{\cdot} + e^{\cdot} \quad (14a)$$

$$V_O^{\cdot} \leftrightarrow V_O^{\cdot\cdot} + e^{\cdot} \quad (14b)$$

The formation of oxygen vacancies (OVs) can be created by three different charge states: the neutral state (V_O), which is capable to imprison two electrons and is neutral in the lattice, the single ionized state ($V_O^{\cdot}$) and the double ionized state ($V_O^{\cdot\cdot}$), which does not imprison any electrons, can be thermally activated, thus improving the conduction process.[56]

In addition, our E_a results for grains 0.364 eV are very close to the activation energy of the ion conductivity induced by single ionized OVs, while the E_a values for grain boundaries 0.638 eV are very close to the activation energy of ionic conductivity induced by doubly ionized OVs in perovskite and tungsten bronze type ferroelectric oxides reported by many authors.[10,20,32,36,57,58] Therefore, we can reasonably conclude that the conducting species in $Ba_5CaTi_{1.94}Zn_{0.06}Nb_8O_{30}$ ceramic are single and doubly ionized oxygen vacancies.

3.6. The spectrum of the imaginary and the real part of the impedance

Fig. 7(a) showed the variation of the imaginary part of the impedance Z'' as a function of the frequency at different temperatures for $Ba_5CaTi_{1.94}Zn_{0.06}Nb_8O_{30}$ ceramic. The

Table 5 Parameters obtained from Joncher's plot for $Ba_5CaTi_{1.94}Zn_{0.06}Nb_8O_{30}$ ceramic

Temperature (°C)	σ_{DC} $(\Omega\ m)^{-1}$	A $(\Omega^{-1}\ m^{-1}\ rad^{-s})$	s
340	1.89487×10^{-6}	1.3849×10^{-7}	0.6131
360	2.97653×10^{-6}	2.20445×10^{-7}	0.5748
380	1.36587×10^{-6}	5.74542×10^{-7}	0.4901
400	3.06541×10^{-6}	1.19158×10^{-6}	0.4215
420	1.73255×10^{-6}	1.20669×10^{-6}	0.4081

amplitude of Z'' at the peak position is called Z''_{max} and the corresponding frequency f_{max} is known as the relaxation frequency. The plots indicate that the Z'' values achieve a maximum peak Z''_{max} and that the value of Z''_{max} moves to higher frequencies with increasing temperature. The relaxation frequency f_{max} was small at low temperatures; this implies that mobile charge carriers (OVs) take a long time to move from one site to another.[31]

To confirm the possible contribution of grain and grain boundary, the Z''_{max} peak of the imaginary part of impedance was decomposed by Gaussian–Lorentzian curve fit at 420 °C (the insets of Fig. 7a). It is an effective strategy for identifying the dielectric responses from grain, grain boundary and electrode effect although with very small differences.[35,59] The Z''_{max} peak is the result of two overlapping peaks. The peak in blue represents the grain contribution, while the peak in green represents the grain boundary contribution. This result has been confirmed by fitting the Nyquist plots with a circuit corresponding to the contribution of grain and grain boundary (see Fig. 5b).

Fig. 7(b) presents the evolution of the real part of the impedance Z' with frequency at different temperatures. It can be seen that the amplitude of Z' decreases with increasing frequency and temperature, indicating an increase in AC conductivity with increasing temperature and frequency.[60] At low frequencies, the real part of the impedance Z' has a high value due to the different types of polarisation present in these materials, such as dipolar, atomic, ionic, electronic, *etc.* But at the higher frequency, the dipolar orientation and the interfacial polarization have decreased, resulting in a constant value of the real part of the impedance Z'.[61] The decrease in the value of Z' with increasing temperature indicated the negative temperature coefficient of resistance (NTCR) behavior.[56,62]

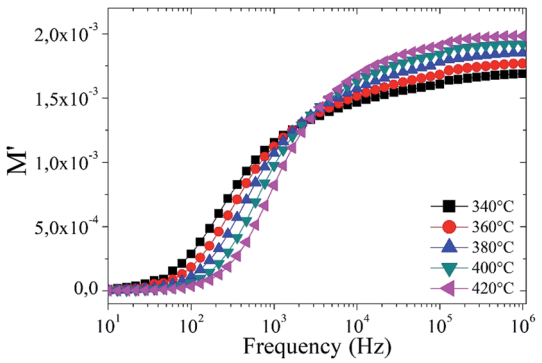

Fig. 8 Real part of the module as a function of frequency for $Ba_5CaTi_{1.94}Zn_{0.06}Nb_8O_{30}$ ceramic.

3.7. Module spectroscopy study

The complex analysis of the dielectric modulus is a practical tool for studying electrical transport phenomena in ceramics and for distinguishing the microscopic processes responsible for dielectric relaxation.[63] The complex dielectric modulus, M^*, is given by the inverse of the complex dielectric constant

$$M^* = 1/\varepsilon^* = j\omega C_0 Z^* = M' + jM'' \quad (15)$$

where M' and M'' are respectively the real and imaginary part of the dielectric module, $C_0 = \frac{\varepsilon_0 A}{d}$ is the geometric capacitance (where ε_0 = vacuum permittivity, A = surface, d = thickness).

The real and imaginary parts of the complex module are expressed as follows

$$M' = \frac{\varepsilon'}{\varepsilon'^2 + \varepsilon''^2};\ M'' = \frac{\varepsilon''}{\varepsilon''^2 + \varepsilon''^2} \quad (16)$$

where ε' and ε'' are respectively the real and imaginary part of the dielectric permittivity.

Fig. 8 illustrates the variation of the real part of the module M' as a function of frequencies at different temperatures. It can

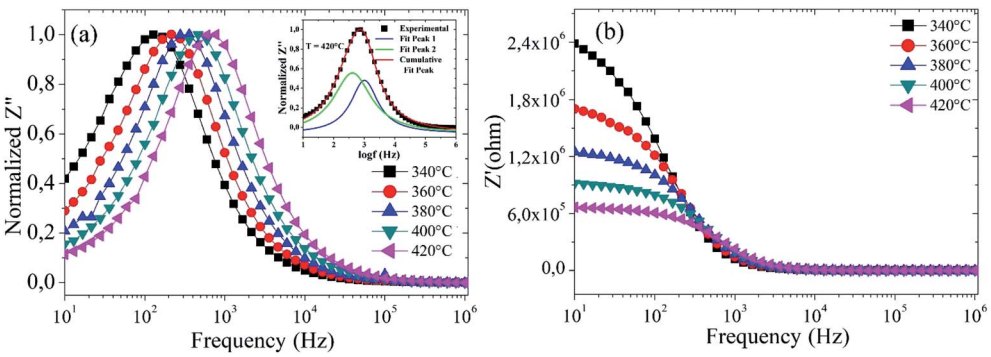

Fig. 7 Variation of (a) the imaginary part (Z''), and (b) the real part (Z') of impedance with frequency at different temperatures for $Ba_5CaTi_{1.94}Zn_{0.06}Nb_8O_{30}$ ceramic.

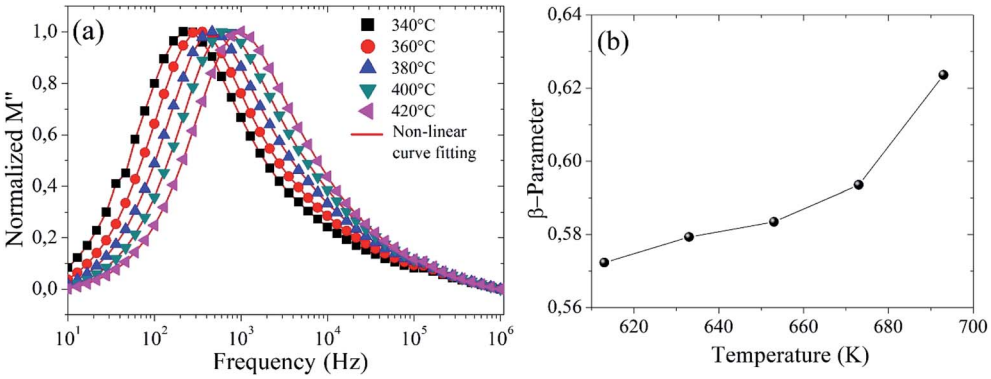

Fig. 9 (a) Imaginary part of the module as a function of frequency, and (b) the plot of β-parameter *versus* temperature for $Ba_5CaTi_{1.94}Zn_{0.06}Nb_8O_{30}$ ceramic.

be observed that in the low frequency region, M' is near to zero, but as the frequency increases, M' continuously increases and closes to saturation after a particular frequency. The saturation in M' is attributed to the conduction mechanism due to the motion of the available charge carriers (OVs).[64,65] However, the increase in temperature enhances the mobility of the charge carriers, so that the overall saturation of M' increases with temperature.

The variation of the imaginary part of the module as a function of frequency is shown in Fig. 9(a). Three types of regions were observed. The first one is the low frequency region below the maximum of the peak of the modulus $M''(2\pi f_{\max}^{M''}\tau_{M''} < 1)$, where charge carriers can move at long distances, *i.e.* they can hop from one site to the neighbouring site (long-distance hopping).[66] The second region is the high-frequency region above the peak maximum of the M'' modulus $(2f_{\max}^{M''}\tau_{M''} > 1)$, where most of the charge carriers have imprisoned in their potential wells, they move over a short distance and can only make a localized movement inside the well.[67] The last region was at the top of the peak of module $M''(2\pi f_{\max}^{M''}\tau_{M''} = 1)$, where the transition from long-distance to short-distance mobility happens.

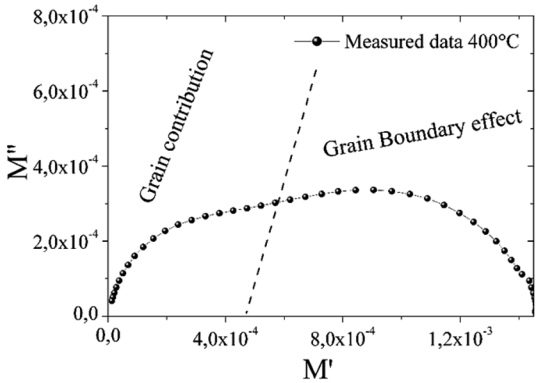

Fig. 10 Complex module diagram (M'' *vs.* M') for $Ba_5CaTi_{1.94}Zn_{0.06}Nb_8O_{30}$ at 400 °C.

An asymmetric broadening of the peaks is also observed in the relaxation peaks $(M''_{\max})$, which indicates the existence of a stretched exponent parameter (β) to identify the type of relaxation process in $Ba_5CaTi_{1.94}Zn_{0.06}Nb_8O_{30}$ ceramic. *i.e.* Debye or non-Debye type relaxation. To verify this, the stretch coefficient (β) is estimated by fitting the imaginary part of M'' derived from the modified Kohlrausch–Williams–Watts (KWW) function proposed by Bergma[68]

$$M'' = \frac{M''_{\max}}{(1-\beta) + \frac{\beta}{1+\beta}\left[\beta\left(\frac{f_{\max}}{f}\right) + \left(\frac{f}{f_{\max}}\right)^{\beta}\right]} \quad (17)$$

where, $M''_{\max}$ is the maximum value of M'', and $f_{\max}$ is the corresponding maximum frequency. For an ideal Debye type relaxation, $\beta = 1$ and for non-Debye type relaxation, (β) lies between 0 and 1 $(0 < \beta < 1)$. The results presented in the Fig. 9(b) suggest that the value of (β) increases with increasing temperature, *i.e.*, from $\beta = 0.5723$ to 0.6236, which confirms that the relaxation process is non-Debye type in $Ba_5CaTi_{1.94}Zn_{0.06}Nb_8O_{30}$ ceramic.

The complex modulus spectrum of M'' *vs.* M' at 400 °C for the compound $Ba_5CaTi_{1.94}Zn_{0.06}Nb_8O_{30}$ gives half circles as shown in Fig. 10. The figure clearly shows two semicircles. The first semicircle at a lower frequency is due to the effect of grains, while the second semicircle at a higher frequency is due to grain boundary effect.[20] This behavior was not visualized by the Nyquist plot (Fig. 5a).

4. Conclusion

$Ba_5CaTi_{1.94}Zn_{0.06}Nb_8O_{30}$ ceramic was obtained *via* the conventional solid-phase reaction. Analysis of the XRD data by the Rietveld refinement showed a quadratic bronze structure with the space group *P4bm* and confirmed the formation of oxygen vacancies. The off-centre displacement of the Ti/Nb/Zn cations along the *c*-axis presented in both octahedrons $Ti/Zn/Nb(1)O_6$ and $Ti/Zn/Nb(2)O_6$. A more important distortion has appeared in the $Ti/Zn/Nb(2)O_6$ than in the $Ti/Zn/Nb(1)O_6$ octahedron. The SEM images showed a homogeneous

microstructure composed of unequal sized grains, high densification, and low porosity. The average grain size was 1.39 μm. The dielectric constant decreases with increasing frequency, and dielectric losses increase with increasing temperature in the low frequency region because of the orientation of the dipole along the field which is facilitated by increasing temperature. The compound exhibited a diffuse type of ferroelectric–paraelectric phase transition having non-relaxor behavior with a T_c of 262 °C. Electrical parameters such as the real and imaginary part of impedance, AC/DC conductivity, the real and imaginary part of modulus as a function of frequency and temperature were studied by impedance spectroscopy. The experimental data of the Nyquist plot has been successfully explained with the help of theoretical simulation, and it was found that grains and grain boundaries both contributed in the conduction process in $Ba_5CaTi_{1.94}Zn_{0.06}Nb_8O_{30}$ ceramic. It also reveals that the resistance of the grains and grain boundaries decreases with increasing temperature, indicating the negative temperature coefficient of resistance (NTCR) behavior. The values of parameter "*s*" obtained from fitting the Jonscher's power law, suggested Correlated Barrier Hopping (CBH) mechanism for charge carriers. Two different activation energy regions were determined by fitting the Arrhenius formula at high temperature, which are 0.364 eV for the grains and 0.638 eV for the grain boundaries, suggesting that single and double ionized oxygen vacancies (OVs) are responsible for electrical conduction in $Ba_5CaTi_{1.94}Zn_{0.06}Nb_8O_{30}$ ceramic. The asymmetric nature of imaginary part of modulus indicated non-Debye type relaxation.

Finally, these preliminary results suggest that the addition of 3% zinc in the $Ba_5CaTi_2Nb_8O_{30}$ ceramic reduces the volume of the lattice, the size of the grains and also leads to a decrease of the Curie temperature from 316 °C to 262 °C, and suggest that Zn-doped $Ba_5CaTi_2Nb_8O_{30}$ ceramic are very attractive for basic science and technological applications.

The analysis of ferroelectric and piezoelectric properties is the subject of our next article, in addition we will study the influence of the concentration of zinc and other dopants on the structural, electrical and ferroelectric properties of $Ba_5CaTi_2Nb_8O_{30}$ ceramic.

Conflicts of interest

There are no conflicts to declare.

Acknowledgements

We are very grateful to "Centre Européen de la Céramique Limoges" for their help and support in the process of samples testing in this work. We thank greatly the anonymous reviewers for their careful review and valuable suggestions on the manuscript. Department of Chemistry – Multidisciplinary Faculty (FPN), is acknowledged for practical assistance with the recording of the spectral analysis.

References

1 S. T. Zhang, G. Yuan, J. Chen, Z. B. Gu, B. Yang, J. Yin and W. Cao, *J. Am. Ceram. Soc.*, 2013, **96**, 555–560.
2 X. L. Zhu, K. Li and X. M. Chen, *J. Am. Ceram. Soc.*, 2014, **97**, 329–338.
3 D. C. Arnold and F. D. Morrison, *J. Mater. Chem.*, 2009, **19**, 6485–6488.
4 C. Huang, K. Li, X. Liu, X. Zhu and X. Chen, *J. Am. Ceram. Soc.*, 2014, **97**, 507–512.
5 E. Castel, P. Veber, M. Albino, M. Velázquez, S. Péchev, D. Denux, J.-P. Chaminade, M. Maglione and M. Josse, *J. Cryst. Growth*, 2012, **340**, 156–165.
6 Y. Yao and C. Mak, *J. Alloys Compd.*, 2012, **544**, 87–93.
7 M. Prades, H. Beltrán, N. Masó, E. Cordoncillo and A. R. West, *J. Appl. Phys.*, 2008, **104**, 104118.
8 I. Levin, M. C. Stennett, G. C. Miles, D. I. Woodward, A. R. West and I. M. Reaney, *Appl. Phys. Lett.*, 2006, **89**, 122908.
9 Z. Guo, S. Wu, C. Hu, L. Liu and L. Fang, *J. Alloys Compd.*, 2019, **773**, 470–481.
10 S. Wu, C. Sun, X. Yang, C. Hu, L. Liu and L. Fang, *Ceram. Int.*, 2020, **46**, 9240–9248.
11 Q. Chen, F. Gao, J. Xu, S. Cao, Y. Guo and G. Cheng, *Ceram. Int.*, 2019, **45**, 9967–9976.
12 Y. Shi, F. Yang, C. Zhao, Y. Huang, M. Li, Q. Zhou, Q. Li, Z. Li, J. Liu and T. Wei, *J. Phys. Chem. Solids*, 2019, **124**, 130–136.
13 K. Chandramouli, P. Viswarupachary and K. Ramam, *J. Mater. Sci.: Mater. Electron.*, 2009, **20**, 977–983.
14 X. L. Zhu, X. Q. Liu and X. M. Chen, *J. Am. Ceram. Soc.*, 2011, **94**, 1829–1836.
15 K. Li, X. L. Zhu, X. Q. Liu and X. M. Chen, *Appl. Phys. Lett.*, 2012, **101**, 042906.
16 Z. Xiao-Li and C. Xiang-Ming, *Chin. Phys. Lett.*, 2014, **31**, 015201.
17 T. Rojac, M. Kosec, B. Budic, N. Setter and D. Damjanovic, *J. Appl. Phys.*, 2010, **108**, 074107.
18 H. Ma, K. Lin, L. Liu, B. Yang, Y. Rong, J. Chen, J. Deng, S. Kawaguchi, K. Kato and X. Xing, *RSC Adv.*, 2015, **5**, 76957–76962.
19 R. Maier, J. Cohn, J. Neumeier and L. A. Bendersky, *Appl. Phys. Lett.*, 2001, **78**, 2536–2538.
20 S. Rani, N. Ahlawat, R. Punia, K. M. Sangwan and P. Khandelwal, *Ceram. Int.*, 2018, **44**, 23125–23136.
21 Z. Guo, Q. Zhu, S. Wu, C. Hu, L. Liu and L. Fang, *Ceram. Int.*, 2018, **44**, 7700–7708.
22 Z. Zhou, Y. Li, L. Yang, X. Dong and H. Yan, *Appl. Phys. Lett.*, 2007, **90**, 212908.
23 B. L. Deng, X. L. Zhu, X. Q. Liu and X. M. Chen, *RSC Adv.*, 2017, **7**, 27370–27376.
24 S. Fei Liu, Y. Jun Wu, J. Li and X. Ming Chen, *Appl. Phys. Lett.*, 2014, **104**, 082912.
25 M. Prades, N. Masó, H. c. Beltrán, E. Cordoncillo and A. R. West, *Inorg. Chem.*, 2013, **52**, 1729–1736.
26 S. Jindal, S. Devi, M. Batoo, G. Kumar and A. Vasishth, *Phys. B*, 2018, **537**, 87–92.

27 B. Behera, P. Nayak and R. Choudhary, *Mater. Chem. Phys.*, 2007, **106**, 193–197.
28 P. Ganguly and A. Jha, *Phys. B*, 2010, **405**, 3154–3158.
29 A. K. Behera, N. Mohanty, S. Satpathy, B. Behera and P. Nayak, *Acta Metall. Sin.*, 2015, **28**, 847–857.
30 P. Gupta, P. Mahapatra and R. Choudhary, *J. Phys. Chem. Solids*, 2020, **137**, 109217.
31 S. Kumar, R. Kurchania and A. Kumar, *Ceram. Int.*, 2019, **45**, 17137–17143.
32 M.-D. Li, X.-G. Tang, S.-M. Zeng, Y.-P. Jiang, Q.-X. Liu, T.-F. Zhang and W.-H. Li, *J. Materiomics*, 2018, **4**, 194–201.
33 A. Yadav, S. P. Mantry, M. Fahad and P. Sarun, *Phys. B*, 2018, **537**, 290–295.
34 V. Petříček, M. Dušek and L. Palatinus, *Zeitschrift für Kristallographie - Crystalline Materials*, 2014, **229**, 345–352.
35 S. Rani, N. Ahlawat, R. Punia, K. M. Sangwan and S. Rani, *Ceram. Int.*, 2018, **44**, 5996–6001.
36 B. Arya and R. Choudhary, *Ceram. Int.*, 2020, **46**, 4222–4234.
37 J. Joshi, D. Kanchan, M. Joshi, H. Jethva and K. Parikh, *Mater. Res. Bull.*, 2017, **93**, 63–73.
38 X. Chen, Y. Sun and X. Zheng, *J. Eur. Ceram. Soc.*, 2003, **23**, 1571–1575.
39 C. Hu, Z. Sun, Q. Zhu, L. Fang and L. Liu, *J. Mater. Sci.: Mater. Electron.*, 2015, **26**, 515–520.
40 S. Nath, S. K. Barik and R. Choudhary, *J. Mater. Sci.: Mater. Electron.*, 2016, **27**, 8717–8724.
41 S. M. Pilgrim, A. E. Sutherland and S. R. Winzer, *J. Am. Ceram. Soc.*, 1990, **73**, 3122–3125.
42 I. W. Kim, C. W. Ahn, J. S. Kim, T. K. Song, J.-S. Bae, B. C. Choi, J.-H. Jeong and J. S. Lee, *Appl. Phys. Lett.*, 2002, **80**, 4006–4008.
43 P. Ganguly, S. Devi, A. Jha and K. Deori, *Ferroelectrics*, 2009, **381**, 111–119.
44 D. C. Sinclair and A. R. West, *J. Appl. Phys.*, 1989, **66**, 3850–3856.
45 H. Ali, S. Karim, M. Rafiq, K. Maaz, A. ur Rahman, A. Nisar and M. Ahmad, *J. Alloys Compd.*, 2014, **612**, 64–68.
46 M. S. Abouzari, F. Berkemeier, G. Schmitz and D. Wilmer, *Solid State Ionics*, 2009, **180**, 922–927.
47 J. R. Macdonald and E. Barsoukov, *History*, 2005, **1**, 1–13.
48 J. R. Macdonald, *Solid State Ionics*, 1984, **13**, 147–149.
49 A. K. Jonscher, *J. Phys. D: Appl. Phys.*, 1999, **32**, R57.
50 K. Funke, *Solid State Ionics*, 1988, **28**, 100–107.
51 S. S. Shah, K. Hayat, S. Ali, K. Rasool and Y. Iqbal, *Mater. Sci. Semicond. Process.*, 2019, **90**, 65–71.
52 S. Elliott, *Adv. Phys.*, 1987, **36**, 135–217.
53 R. Muhammad, A. Khesro and M. Uzair, *J. Electron. Mater.*, 2016, **45**, 4083–4088.
54 J. Scott and M. Dawber, *Appl. Phys. Lett.*, 2000, **76**, 3801–3803.
55 U. Balachandran, B. Odekirk and N. Eror, *J. Mater. Sci.*, 1982, **17**, 1656–1662.
56 T. Badapanda, V. Senthil, S. Rout, L. Cavalcante, A. Z. Simões, T. Sinha, S. Panigrahi, M. De Jesus, E. Longo and J. A. Varela, *Curr. Appl. Phys.*, 2011, **11**, 1282–1293.
57 G. Singh, V. Tiwari and P. Gupta, *J. Appl. Phys.*, 2010, **107**, 064103.
58 L. Liu, Y. Huang, Y. Li, M. Wu, L. Fang, C. Hu and Y. Wang, *Phys. B*, 2012, **407**, 136–139.
59 J. C. Abrantes, J. A. Labrincha and J. R. Frade, *Mater. Res. Bull.*, 2000, **35**, 727–740.
60 T. Badapanda, V. Senthil, S. Rout, S. Panigrahi and T. Sinha, *Mater. Chem. Phys.*, 2012, **133**, 863–870.
61 S. Hosseini, K. Ranjbar, R. Dehmolaei and A. Amirani, *J. Alloys Compd.*, 2015, **622**, 725–733.
62 K. S. Cole and R. H. Cole, *J. Chem. Phys.*, 1941, **9**, 341–351.
63 Y. Wong, J. Hassan and M. Hashim, *J. Alloys Compd.*, 2013, **571**, 138–144.
64 B. Chowdari and R. Gopalakrishnan, *Solid State Ionics*, 1987, **23**, 225–233.
65 K. Padmasree, D. Kanchan and A. Kulkarni, *Solid State Ionics*, 2006, **177**, 475–482.
66 S. Brahma, R. Choudhary and A. K. Thakur, *Phys. B*, 2005, **355**, 188–201.
67 S. K. Barik, R. Choudhary and A. Singh, *Adv. Mater. Lett.*, 2011, **2**, 419–424.
68 R. Bergman, *J. Appl. Phys.*, 2000, **88**, 1356–1365.

